Quantum valley and subvalley Hall effect in large-angle twisted bilayer graphene

Chiranjit Mondal,[1,2,*] Rasoul Ghadimi ®,[1,2,*] and Bohm-Jung Yang[1,2,3,†]

[1]*Department of Physics and Astronomy, Seoul National University, Seoul 08826, Republic of Korea*
[2]*Center for Theoretical Physics (CTP), Seoul National University, Seoul 08826, Republic of Korea*
[3]*Center for Correlated Electron Systems, Institute for Basic Science (IBS), Seoul 08826, Republic of Korea*

We study the quantum valley Hall effect and related domain wall modes in twisted bilayer graphene at a large commensurate angle. Due to the quantum valley and subvalley Hall effect, a small deviation from the commensurate angle generates two-dimensional conducting network patterns composed of one-dimensional domain walls, which can host non-Fermi-liquid behavior within an accessible temperature range. The domain wall modes can be manipulated using an external electric field and layer shifting, manifesting the physics of the celebrated Haldane and Semenoff models for the subvalley Dirac cones, living on the domain walls. These findings open up an alternative direction towards realizing the emergence and manipulation of topological quantum valley and subvalley Hall states and possible applications in valleytronics. Our theory can be generalized to many twisted bilayer systems, including twisted graphene, twisted α-graphene, and twisted kagome bilayers at large-angle rotation.

Introduction. Small-angle twisted bilayer graphene (TBG) has become an active research avenue after the discovery of various correlated states such as superconductor, Mott insulator, quantum fractal phase, etc. [1–17]. Many of these intriguing phenomena appear at certain rotation angles, coined magic angles, at which the electronic kinetic energy is minimized [18–21]. Interestingly, contrary to the early prediction of layer decoupling at large twist angles [22], recent studies have observed fascinating physical properties arising from interlayer coupling even at large rotation angles, including higher-order topology [23,24], geometrical frustration [25], flat bands [25], hypermagic angles [26], and nontrivial optical response [27].

The low-energy band structure of large-angle TBG is crucially affected by the higher-order Fourier components of the interlayer coupling [28,29]. Explicitly, according to Refs. [28,29], commensurate-angle TBGs can be classified into sublattice-exchange-odd (SEO) and sublattice-exchange-even (SEE) configurations. SEE has only one stacking configuration, similar to AA-stacked bilayer graphene (BLG); hence we call it the effective AA (EAA) structure. The energy spectrum of EAA possesses gapped band structures that host crystalline and higher-order topological insulators [23,24]. In contrast, SEO can have two types of stacking structures similar to the Bernal-stacked BLG. We name them the effective AB (EAB) and effective BA (EBA) configurations, respectively. One fascinating phenomenon observed in AB and BA BLG is the quantum valley Hall effect (QVHE) [30–43]. Considering the extensive research activities involving the QVHE and its great potential for device applications, it is

highly desirable to extend related topological phenomena to other two-dimensional material setups. Especially, if such a valley-dependent functionality can also be achieved in twisted BLG, the tunability of the twisted structure would facilitate further rapid development of valleytronics applications.

In this Research Letter, we study the valley-dependent topological properties of TBG with a large twist angle. In particular, we establish the bulk-edge or bulk-domain wall correspondence using theoretical models and realistic *ab initio* computations based on density functional theory (DFT; see Supplemental Material (SM) [44] for the computational details). We found that an out-of-plane electric field (E-field) opens up a topological gap in EAB and EBA TBG. In the presence of U(1) valley symmetry (i.e., without valley mixing), EAB TBG and EBA TBG support gapless domain wall (DW) modes between two distinct configurations with different valley Chern numbers (VCNs). The VCN C_v is defined as integrating the Berry curvature around a given valley. This QVHE and its DW modes can be tuned by applying an external E-field, applying a twisting angle, and shifting one layer with respect to another. We found that the shifting works as an emergent E-field that competes with the external E-field to produce subvalley Dirac cones and the corresponding subvalley Hall effect. This emergent phenomenon is akin to the topological physics of the Haldane model in single-layer graphene. Namely, two subvalleys experience a Haldane mass that emerges from the layer shifting and a Semenoff mass that is induced by an external E-field. The competition between these Haldane and Semenoff subvalley masses gives rise to tunable DW modes in large-angle TBG.

Structure and VCN. In the following, we consider a commensurate angle $\theta = 38.21°$. However, our conclusions also remain the same for other large commensurate angles. The lattice structure of EAB and EAA configurations for 38.21°
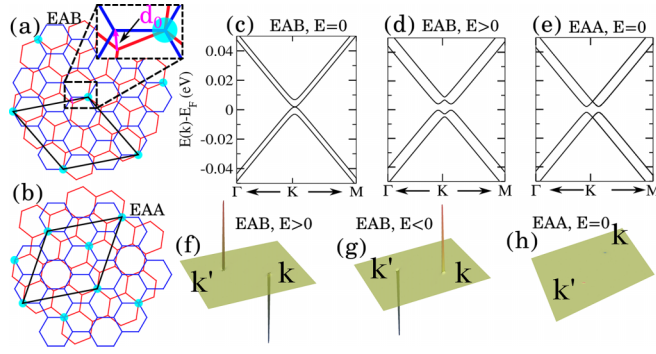

FIG. 1. The lattice structure of (a) the EAB configuration at twist angle 38.21° and (b) the EAA configuration obtained by a shift $\mathbf{d} = \{0, 2d_0\}$ from the EAB configuration. Blue and red lines represent the top and bottom layers, respectively. Cyan discs represent the eclipsed atoms of the two layers. The primitive unit cell is shown by the solid black line. (c) and (d) Band structures of the EAB structure when $E = 0$ (c) and $E \neq 0$ (d). $E \neq 0$ opens up a gap at the K and K' valleys. (e) Band structure of the EAA structure. (f) and (g) Berry curvature distributions of the EAB structure under $E > 0$ (f) and $E < 0$ (g). (h) Vanishing Berry curvature of the EAA structure.

is shown in Figs. 1(a) and 1(b). Note that EAA can be constructed from EAB by shifting one layer with respect to the other by a shift vector $\mathbf{d} = \{0, 2d_0\}$. The DFT band structure of EAB in the absence of an E-field (i.e., $E = 0$) shows gapless quadratic bands touching at each valley K or K' of the superlattice Brillouin zone [see Fig. 1(c)]. However, turning on the E-field gaps out those quadratic bands touching [see Fig. 1(d)]. In Figs. 1(f) and 1(g), we plot the Berry curvature distribution of EAB under $\pm E$, which shows that the gapped Dirac cones act as the hotspot of the Berry curvature. The VCN changes its sign upon reversing the direction of the E-field or changing the valley, i.e., $C_v = \eta\,\mathrm{sgn}(E)$ (see SM for the derivation), where $\eta = \pm 1$ represents the valley index. In contrast, the band structure of the EAA configuration is always gapped irrespective of the presence or absence of E [see Fig. 1(e)]. However, EAA does not show any Berry curvature because of the underlying $\mathcal{C}_{2z}\mathcal{T}$ symmetry, where $\mathcal{C}_{2z} : \{x, y, z\} \rightarrow \{-x, -y, z\}$ and $\mathcal{T}$ are twofold rotation and time-reversal symmetries, respectively. This is because $\mathcal{C}_{2z}\mathcal{T}$ symmetry enforces the reality of the wave functions and vanishing Berry curvature [54–56].

Domain wall modes. In general, gapless modes appear at the edge or DW between two systems with distinct topological invariants. As such, we expect the edge or DW modes to appear at the edges or DW between two configurations with different VCNs. Also, the presence of opposite VCNs from opposite valleys forces the edge or DW modes to propagate with opposite velocities. Furthermore, the absolute change in the VCN, $\Delta \mathcal{C}_v = |\mathcal{C}_v^A - \mathcal{C}_v^B|$, between two regions A and B is equal to the number of DW modes between those regions. For instance, in Fig. 2(a), we consider a TBG ribbon with an EAB configuration. We then apply opposite E-fields on the two sides of the system. In this case, as $\Delta \mathcal{C}_v = \pm 2$ for the K and K' valleys, respectively, the system hosts two counterpropagating modes in each valley. We numerically confirm the existence of DW and edge modes in the energy
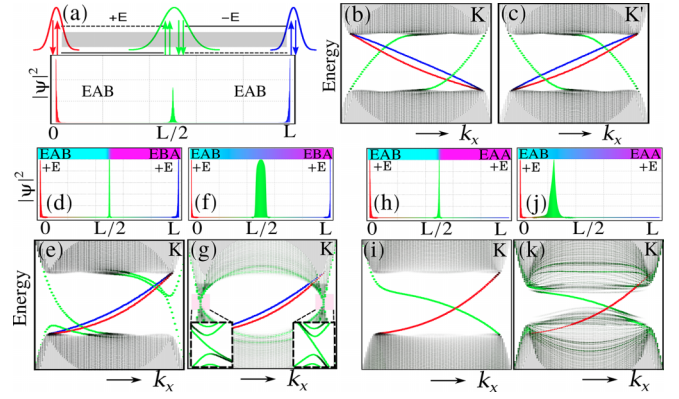

FIG. 2. Edge and DW modes under different E-field and DW configurations. The green (blue or red) color represents the DW (edge) modes. (a) A DW is created in EAB by changing the sign of E (i.e., $+E$ and $-E$) across the system. Wave functions are strongly localized at the DW ($L/2$) and edges (0 and L). (b) and (c) Energy dispersion along the DW and edges near each valley K or K' for a ribbon geometry with periodicity along the DW. (d) and (f) DWs are created sharply (d) and smoothly (f) between the EAB and EBA (i.e., alternate stacking configuration) under $+E$. Corresponding localized modes are shown in (e) and (g) for the K valley. (h) and (j) Sharp (h) and smooth (j) DWs are created between the EAB and EAA under $+E$. For the smooth junction in (j), the wave function is localized near EAB. Corresponding edge and DW states are shown in (i) and (k) for the K valley. The color bars in (d), (f), (h), and (j) represent how the DWs are created, sharply or smoothly, between two different configurations as represented by cyan and magenta colors.

spectrum calculation, where we assume the periodicity along the boundary between two regions, as shown in Figs. 2(b) and 2(c); the DW (edge) modes are shown in green (red or blue) (see SM for details of the tight-binding calculations). We plot the corresponding wave functions in Fig. 2(a), which are exponentially localized at the DW and edges, respectively. The existence of edge states can be explained by the change in the VCN between EAB or EBA and the vacuum. For instance, EAB obtains $|\mathcal{C}_v| = 1$ under the E-field, which gives $\Delta \mathcal{C}_v = 1$ between EAB and the vacuum. Note that the change in the VCN between EAB and the vacuum is of the same sign for both the left and right edges. This is because the sign of the VCN changes on two sides by the opposite sign of the E-field. Therefore the states at the two edges obtain the same propagation direction. Furthermore, as the change in the VCN between EAB and EBA under the same E-field is equal to $\Delta \mathcal{C}_v = \pm 2$, we expect similar edge and DW modes localized between them [see Figs. 2(d) and 2(e)]. The existence of DW modes is very robust as their appearance does not depend on the detailed chemistry of the DW. For demonstration, we construct a ribbon of TBG and then slowly shift one layer with respect to the other layer, to construct a smooth DW between EAB and EBA [see Fig. 2(f)]. We observe two in-gap DW modes and edge modes as shown in the insets of Fig. 2(g), similar to Fig. 2(e).

The existence of DW modes in the EAB or EBA configuration is similar to the case of AB-stacked BLG. However, in contrast to gapless AA-stacked BLG, the EAA configuration of commensurate TBG is gapped, and $C_v = 0$. Therefore one
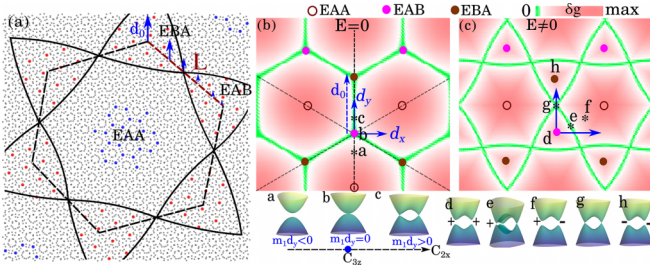
FIG. 3. (a) TBG with a small twisting $\delta\theta_c$ from the commensurate angle $\theta_c = 38.21°$. The local configurations of EAA and EAB or EBA (separated by a black solid line) can be traced by tracking the coordination of eclipsed atoms (atoms in two layers stacked on top, shown by red and blue dots) which form a triangular (hexagonal) coordination in the EAA (EAB or EBA) region. (b) and (c) Maps of the direct energy gap δg of local structures in real space as a function of the shift vector $\mathbf{d}$ for $E = 0$ (b) and $E \neq 0$ (c). The vector d_0 in (b) has a unique correspondence with L in (a) as shown by the increasing d_0 (blue arrows) along the line with length $L = l/[2\sin(\delta\theta_c/2)]$ in (a) where l represents the lattice constant of EAA or EAB. The positions of local structures with different $\mathbf{d}$ vectors are labeled as positions a, b, and c in (b) and positions d, e, f, g, and h in (c). The energy dispersions in momentum space near K and K' corresponding to the local structures are shown in the bottom panel of (b) and (c). The $\pm$ symbols represent the sign of the Berry curvature of the gapped Dirac cones.

can imagine that EAA effectively behaves as a vacuum state. Consequently, by creating a DW between EAA and EAB, we expect the appearance of DW modes between them. In Figs. 2(h) and 2(i), indeed, we confirm the existence of one DW mode at the center of the system. Additionally, as is shown in Figs. 2(h) and 2(i), only the edge located on the EAB side supports edge modes, while the EAA edge does not support any edge modes. This is in accordance with the nonzero (zero) VCN of EAB (EAA). Similar to the EAB-EBA setup in Fig. 2(f), a DW between EAB and EAA, created by smoothly changing the local configuration, also hosts DW modes as shown in Figs. 2(j) and 2(k). However, the position of the DW mode wave functions is located closer to the EAB region [see Fig. 2(j)].

Incommensurate structure and domain wall network. When two layers are slightly rotated from a commensurate angle θ_c, it generally breaks the commensurability of the lattice over a large length scale in the lattice (see SM). However, such an incommensurate system locally resembles a commensurate configuration [see Fig. 3(a)] that can be constructed by a certain amount of shifting of one layer with respect to the other layer, where the nearby local structures are connected by smooth shifting [26]. Moreover, the local structural environment could be large enough to construct momentum space locally [18]. In the following, we study the existence of DW modes based on the energy spectrum of the local structures. First, we construct the commensurate TBG Hamiltonian at $\theta_c = 38.21°$, and then the Hamiltonian of the local structure is constructed by using the appropriate shift vector $\mathbf{d}$. In TBG, the effective low-energy Hamiltonian comprises two parts. The intralayer part can be represented by the Dirac Hamiltonian $H_{1,2} = -i\nu(\sigma_x k_x + \sigma_y k_y)$, where ν is the Fermi velocity

and σ_i represents the Pauli matrices. The interlayer coupling part Hamiltonian for $\theta_c = 38.21°$ is written as (see SM for the derivation)

$$H^{\alpha\beta}_{\mathbf{k},\tilde{\mathbf{k}}} = t_{\mathbf{k}+\mathbf{G}} \sum_{i=1}^{3} e^{i\mathbf{G}_i \cdot (\tau^\alpha + \mathbf{d})} e^{-i\tilde{\mathbf{G}}_i \cdot \tau^\beta}, \quad (1)$$

where α and β represent the sublattice index with positions $\tau_i(i = \alpha, \beta)$; $\mathbf{G} = \sum n_i \mathbf{b}_i$ and $\tilde{\mathbf{G}} = \sum \tilde{n}_i \tilde{\mathbf{b}}_i$ are the reciprocal lattice vectors for the two layers, respectively; and $t_{\mathbf{k}+\mathbf{G}}$ is the Fourier coefficient of the tight-binding hopping in the momentum space whose amplitude decays rapidly with $|\mathbf{k} + \mathbf{G}|$. The $\mathbf{G}$ and $\tilde{\mathbf{G}}$ vectors that satisfy the momentum conservation process with the largest $|t|$ are given as $(\mathbf{G}_1, \tilde{\mathbf{G}}_1) = (\mathbf{b}_1, \tilde{\mathbf{b}}_1 + \tilde{\mathbf{b}}_2)$, $(\mathbf{G}_2, \tilde{\mathbf{G}}_2) = (-2\mathbf{b}_1 - 2\mathbf{b}_2, -\tilde{\mathbf{b}}_1 - 2\tilde{\mathbf{b}}_2)$, and $(\mathbf{G}_3, \tilde{\mathbf{G}}_3) = (-\mathbf{b}_1 + \mathbf{b}_2, -2\tilde{\mathbf{b}}_1)$. The Hamiltonian for the external E-field is written as $H_E = \text{diag}(E, E, -E, -E)$.

In Figs. 3(b) and 3(c), we show the map of the direct energy gap Δg of the local structures for $E = 0$ and $E \neq 0$ as a function of the shift vector $\mathbf{d}$. When $E = 0$, some local structures possess two important symmetries. They are twofold in-plane ($\mathcal{C}_2$) and threefold out-of-plane ($\mathcal{C}_{3z}$) rotational symmetries. For instance, let us consider a locus of local structures on a line, connecting EAA, EAB, and EBA [vertical dashed line in Fig. 3(b)]. For $E = 0$, all the local structures on this line are $\mathcal{C}_2$ symmetric with an additional $\mathcal{C}_{3z}$ at the positions EAB and EBA. Figure 3(b) shows that the local structure at EAA is gapped, which is also consistent with our DFT calculations, as discussed in Fig. 1(e). However, from the EAA towards the EAB (on the dashed line), the Δg decreases and finally closes at EAB, at which quadratic band crossing appears at the K or K' valley. The energy dispersion near a valley, corresponding to the local structure in positions a and b, is shown in the bottom panel of Fig. 3(b). By further moving towards EBA from EAB, the quadratic band touching split into two Dirac cones, which we call subvalley Dirac cones [see the energy dispersion at a general position c in the bottom panel of Fig. 3(b)]. These subvalley Dirac cones are protected by the underlying $\mathcal{C}_2$ symmetry and finally merge together at EBA to form a quadratic band touching.

For a better understanding of the DW physics, we derive a low-energy Hamiltonian up to the second order in the momentum under an external E-field considering a slight shift from the EAB on the vertical dashed line (i.e., $d_x = 0$), which becomes (see SM for the derivation)

$$H_{0,d_y}(k_x, k_y) = \left(\alpha\left(k_x^2 - k_y^2\right) + m_1 d_y\right)\sigma_x - 2\alpha\, k_x k_y \sigma_y$$
$$+ (E + m_3\, d_y k_y)\sigma_z, \quad (2)$$

where α and m_i ($i = 0, 1, 2, 3$) are the constants. When $E = 0$, the system recovers $\mathcal{C}_2 = \sigma_x$ symmetry, and it supports a gapless spectrum at $k_y = 0$ and $k_x = \pm k_0$, where $k_0 = \sqrt{m_1 d_y}$. As such, for $m_1 > 0$, two gapless solutions appear only when $d_y > 0$, and no solutions appear for $d_y < 0$. This is in accordance with Fig. 3(b), where gapless configurations only appear for $d_y > 0$, while the local structures for $d_y < 0$ are gapped. The two regions meet each other at EAB ($d_y = 0$) on the vertical dashed line. The quadratic band touching at this point is enforced by the underlying $C_{3z} = e^{i\frac{2\pi}{3}\sigma_z}$ symmetry.

Now, we write an effective Hamiltonian for each subvalley Dirac cone (for $d_y > 0$) as $H_{sv} = k_x \sigma_x + k_y \sigma_y$ sitting at $\pm k_0$. These gapless Dirac cones cannot be gapped out unless the $\mathcal{C}_2$ symmetry is broken by either a nonzero shift along d_x or an E-field E. The d_x and E result in a mass term for these subvalley Dirac cones,

$$\mathcal{M}_{sv} = (E \pm d_x k_0)\sigma_z, \tag{3}$$

where the first mass term comes from E and the second term is related to d_x, which can be interpreted as an emergent electric field. The two subvalley Dirac cones get the same sign of masses by E, akin to the Semenoff mass as in the case of single-layer graphene [57]. However, away from the $\mathcal{C}_2$-symmetric DW configurations (i.e., $d_x \neq 0$), the second term in Eq. (3) induces the opposite sign of masses for the two subvalley Dirac cones, resembling the Haldane mass as in single-layer graphene [58]. This subvalley Haldane mass gives opposite subvalley Chern numbers (sub-VCNs) for two gapped subvalley Dirac cones. The sub-VCN is defined by the integration of the Berry curvature around each gapped subvalley Dirac cone. Note that the sign of the sub-VCN changes when d_x changes its sign about the $d_x = 0$ line. For instance, if the sub-VCNs for two gapped Dirac cones are $(+1/2, -1/2)$ for $d_x > 0$, they are then $(-1/2, +1/2)$ for $d_x < 0$. Therefore the change in the sub-VCN between $d_x < 0$ and $d_x > 0$ is ± 1, which protects the two counterpropagating DW modes at $d_x = 0$. Therefore this system can host a quantum subvalley Hall effect even in the absence of a true external E-field.

In the presence of E, the $\mathcal{C}_2$ symmetry is broken, which gaps out both the subvalley Dirac cones as depicted for positions d and h in Fig. 3(c). According to Eq. (3), as d_x increases, one Dirac cone remains gapped, while the other Dirac cone goes through the gap closing and reopening at the DW when $|E| = |d_x k_0|$ [see positions e and f in Fig. 3(c)]. This gapless Dirac point corresponds to a DW mode, which is also consistent with $\Delta C_v = 1$ between positions d and f in Fig. 3(c). The phase transition resembles the Haldane model with a different sublattice potential (known as the Semenoff mass) in the case of single-layer graphene, where the competition between the Semenoff mass and the Haldane mass dictated the topological phase boundary. Furthermore, at the EAA, two gapped subvalley Dirac cones meet each other and annihilate their underlying Berry curvature and hence the sub-VCN. Note that $\Delta C_v = 2$ between positions d and h (EAB and EBA) in Fig. 3(c), which ensures two DW modes, represented by two gapless Dirac cones at position g [see bottom panel of Fig. 3(b)]. The DW mode between EAB-EBA and EAA in Fig. 3(c) appears closer to the EAB-EBA region, which is consistent with our tight-binding calculation in Fig. 2(j). In contrast, the gapless DW configuration between EAB and EBA [Fig. 3(b)] appears exactly between them, which is consistent with Fig. 2(f).

Discussion. Let us compare the QVHE in large-angle TBG with that in untwisted or small-angle twisted TBG. First, in the presence of an E-field, all the configurations, EAA, EAB, and EBA, are gapped in large-angle commensurate TBG, which makes it distinct from the small-angle twisting, where the AA configuration is gapless even under an E-field. Second, unlike

TABLE I. Number of atoms N, in-plane lattice constant l, and band gap Δ of the EAA configuration for several θ_c with the largest layer coupling at a large angle of rotation.

θ_c (deg)	N	l (Å)	Δ (meV)
38.21	28	6.46	5
32.2	52	8.85	0.1
43.17	76	10.7	0.2
42.1	124	13.67	0.25

the small-angle case, the relaxation effect is insignificant in large-angle twisting. This is because the ground state energy difference (computed using DFT) between AA and AB-BA is $\sim$103 meV/atom whereas it is only 0.14 meV/atom in the case of EAA and EAB-EBA at $\theta_c = 38.21°$. Therefore lattice relaxation makes the AA region shrink into a topological point defect [43] in the small-angle TBG. However, in large-angle TBG, EAA, EAB, and EBA all exist as stable local structures and support the proposed DW states.

Although our theory is generally valid, it is experimentally more significant near a few values of θ_c as the band gap Δ decreases rapidly when the lattice constant l and the number of atoms N of the commensurate unit cell increases as listed in Table I, where we show Δ for four θ_c values with the smallest l and N.

The proposed DW modes can be detected in both scanning tunneling microscopy (STM) and transport measurements. As the size of the DW network is larger than the STM resolution, it can be detected by the STM local density of states and dc optical conductance measurement [39]. Moreover, the two-dimensional (2D) conducting DW network pattern can induce intriguing non-Fermi-liquid behavior above a critical temperature $T_x \sim \frac{\hbar v_f}{k_B L}$, where v_f, $\hbar$, k_B, and L represent the DW Fermi velocity, reduced Planck constant, Boltzmann constant, and length of 1D conducting channels, respectively [59]. In our case, for a rotation $\delta\theta_c = 0.05°$ from $\theta_c = 38.21°$, L is $\sim$740 nm, and computed v_f is $\sim$0.6 × 10⁶ m/s, which gives $T_x \approx 7$ K. As the band gap of EAA is $\sim$5 meV ($\sim$58 K in the temperature scale), the 2D DW network at $\delta\theta_c = 0.05°$ is expected to show 1D non-Fermi-liquid transport from 7 K up to $\sim$58 K.

Finally, we note that our theoretical idea can also be applied to other related structures such as twisted bilayer α-graphene [60] and twisted kagome bilayers [61] (see SM for more details) with more tunability.

[1] Y. Cao, V. Fatemi, S. Fang, K. Watanabe, T. Taniguchi, E. Kaxiras, and P. Jarillo-Herrero, Unconventional superconductivity in magic-angle graphene superlattices, Nature (London) **556**, 43 (2018).

[2] M. Oh, K. P. Nuckolls, D. Wong, R. L. Lee, X. Liu, K. Watanabe, T. Taniguchi, and A. Yazdani, Evidence for unconventional superconductivity in twisted bilayer graphene, Nature (London) **600**, 240 (2021).

[3] M. Yankowitz, S. Chen, H. Polshyn, Y. Zhang, K. Watanabe, T. Taniguchi, D. Graf, A. F. Young, and C. R. Dean, Tuning superconductivity in twisted bilayer graphene, Science **363**, 1059 (2019).

[4] A. Chew, Y. Wang, B. A. Bernevig, and Z.-D. Song, Higher-order topological superconductivity in twisted bilayer graphene, Phys. Rev. B **107**, 094512 (2023).

[5] M. Christos, S. Sachdev, and M. S. Scheurer, Superconductivity, correlated insulators, and Wess-Zumino-Witten terms in twisted bilayer graphene, Proc. Natl. Acad. Sci. USA **117**, 29543 (2020).

[6] B.-B. Chen, Y. Da Liao, Z. Chen, O. Vafek, J. Kang, W. Li, and Z. Y. Meng, Realization of topological Mott insulator in a twisted bilayer graphene lattice model, Nat. Commun. **12**, 5480 (2021).

[7] H. C. Po, L. Zou, A. Vishwanath, and T. Senthil, Origin of Mott Insulating Behavior and Superconductivity in Twisted Bilayer Graphene, Phys. Rev. X **8**, 031089 (2018).

[8] K. Kim, A. DaSilva, S. Huang, B. Fallahazad, S. Larentis, T. Taniguchi, K. Watanabe, B. J. LeRoy, A. H. MacDonald, and E. Tutuc, Tunable moiré bands and strong correlations in small-twist-angle bilayer graphene, Proc. Natl. Acad. Sci. USA **114**, 3364 (2017).

[9] S. Sinha, P. C. Adak, S. Kanthi R. S., B. L. Chittari, L. D. Varma Sangani, K. Watanabe, T. Taniguchi, J. Jung, and M. M. Deshmukh, Bulk valley transport and Berry curvature spreading at the edge of flat bands, Nat. Commun. **11**, 5548 (2020).

[10] S. Bhowmik, B. Ghawri, N. Leconte, S. Appalakondaiah, M. Pandey, P. S. Mahapatra, D. Lee, K. Watanabe, T. Taniguchi, J. Jung, A. Ghosh, and U. Chandni, Broken-symmetry states at half-integer band fillings in twisted bilayer graphene, Nat. Phys. **18**, 639 (2022).

[11] Yu. Saito, J. Ge, L. Rademaker, K. Watanabe, T. Taniguchi, D. A. Abanin, and A. F. Young, Hofstadter subband ferromagnetism and symmetry-broken Chern insulators in twisted bilayer graphene, Nat. Phys. **17**, 478 (2021).

[12] H. S. Arora, R. Polski, Y. Zhang, A. Thomson, Y. Choi, H. Kim, Z. Lin, I. Z. Wilson, X. Xu, J.-H. Chu, K. Watanabe, T. Taniguchi, J. Alicea, and S. Nadj-Perge, Superconductivity in metallic twisted bilayer graphene stabilized by WSe$_2$, Nature (London) **583**, 379 (2020).

[13] J. Y. Lee, E. Khalaf, S. Liu, X. Liu, Z. Hao, P. Kim, and A. Vishwanath, Theory of correlated insulating behaviour and spin-triplet superconductivity in twisted double bilayer graphene, Nat. Commun. **10**, 5333 (2019).

[14] C.-C. Tseng, X. Ma, Z. Liu, K. Watanabe, T. Taniguchi, J.-H. Chu, and M. Yankowitz, Anomalous Hall effect at half filling in twisted bilayer graphene, Nat. Phys. **18**, 1038 (2022).

[15] I. Das, X. Lu, J. Herzog-Arbeitman, Z.-Da. Song, K. Watanabe, T. Taniguchi, B. A. Bernevig, and D. K. Efetov, Symmetry-broken Chern insulators and Rashba-like Landau-level crossings in magic-angle bilayer graphene, Nat. Phys. **17**, 710 (2021).

[16] S. Wu, Z. Zhang, K. Watanabe, T. Taniguchi, and E. Y. Andrei, Chern insulators, van Hove singularities and topological flat bands in magic-angle twisted bilayer graphene, Nat. Mater. **20**, 488 (2021).

[17] K. P. Nuckolls, M. Oh, D. Wong, B. Lian, K. Watanabe, T. Taniguchi, B. A. Bernevig, and A. Yazdani, Strongly correlated Chern insulators in magic-angle twisted bilayer graphene, Nature (London) **588**, 610 (2020).

[18] R. Bistritzer and A. H. MacDonald, Moiré bands in twisted double-layer graphene, Proc. Natl. Acad. Sci. USA **108**, 12233 (2011).

[19] J. M. B. Lopes dos Santos, N. M. R. Peres, and A. H. Castro Neto, Graphene Bilayer with a Twist: Electronic Structure, Phys. Rev. Lett. **99**, 256802 (2007).

[20] S. Shallcross, S. Sharma, E. Kandelaki, and O. A. Pankratov, Electronic structure of turbostratic graphene, Phys. Rev. B **81**, 165105 (2010).

[21] E. Suárez Morell, J. D. Correa, P. Vargas, M. Pacheco, and Z. Barticevic, Flat bands in slightly twisted bilayer graphene: Tight-binding calculations, Phys. Rev. B **82**, 121407(R) (2010).

[22] S. Shallcross, S. Sharma, and O. A. Pankratov, Quantum Interference at the Twist Boundary in Graphene, Phys. Rev. Lett. **101**, 056803 (2008).

[23] M. Kindermann, Topological Crystalline Insulator Phase in Graphene Multilayers, Phys. Rev. Lett. **114**, 226802 (2015).

[24] M. J. Park, Y. Kim, G. Y. Cho, and S. Lee, Higher-Order Topological Insulator in Twisted Bilayer Graphene, Phys. Rev. Lett. **123**, 216803 (2019).

[25] H. K. Pal, S. Spitz, and M. Kindermann, Emergent Geometric Frustration and Flat Band in Moiré Bilayer Graphene, Phys. Rev. Lett. **123**, 186402 (2019).

[26] M. G. Scheer, K. Gu, and B. Lian, Magic angles in twisted bilayer graphene near commensuration: Towards a hypermagic regime, Phys. Rev. B **106**, 115418 (2022).

[27] S. Talkington and E. J. Mele, Electric field tunable band gap in commensurate twisted bilayer graphene, Phys. Rev. B **107**, L041408 (2023).

[28] E. J. Mele, Commensuration and interlayer coherence in twisted bilayer graphene, Phys. Rev. B **81**, 161405(R) (2010).

[29] E. J. Mele, Interlayer coupling in rotationally faulted multilayer graphenes, J. Phys. D: Appl. Phys. **45**, 154004 (2012).

[30] I. Martin, Ya. M. Blanter, and A. F. Morpurgo, Topological Confinement in Bilayer Graphene, Phys. Rev. Lett. **100**, 036804 (2008).

[31] A. Vaezi, Y. Liang, D. H. Ngai, Li Yang, and E.-Ah Kim, Topological Edge States at a Tilt Boundary in Gated Multilayer Graphene, Phys. Rev. X **3**, 021018 (2013).

[32] J. Jung, F. Zhang, Z. Qiao, and A. H. MacDonald, Valley-Hall kink and edge states in multilayer graphene, Phys. Rev. B **84**, 075418 (2011).

[33] G. W. Semenoff, V. Semenoff, and F. Zhou, Domain Walls in Gapped Graphene, Phys. Rev. Lett. **101**, 087204 (2008).

[34] F. Zhang, J. Jung, G. A. Fiete, Q. Niu, and A. H. MacDonald, Spontaneous Quantum Hall States in Chirally Stacked Few-Layer Graphene Systems, Phys. Rev. Lett. **106**, 156801 (2011).

[35] D. Xiao, W. Yao, and Q. Niu, Valley-Contrasting Physics in Graphene: Magnetic Moment and Topological Transport, Phys. Rev. Lett. **99**, 236809 (2007).

[36] Z. Qiao, J. Jung, Q. Niu, and A. H. MacDonald, Electronic highways in bilayer graphene, Nano Lett. **11**, 3453 (2011).

[37] Y. Shimazaki, M. Yamamoto, I. V. Borzenets, K. Watanabe, T. Taniguchi, and S. Tarucha, Generation and detection of pure valley current by electrically induced Berry curvature in bilayer graphene, Nat. Phys. **11**, 1032 (2015).

[38] L. Ju, Z. Shi, N. Nair, Y. Lv, C. Jin, J. Velasco Jr, C. Ojeda-Aristizabal, H. A. Bechtel, M. C. Martin, A. Zettl, J. Analytis, and F. Wang, Topological valley transport at bilayer graphene domain walls, Nature (London) **520**, 650 (2015).

[39] L.-J. Yin, H. Jiang, J.-B. Qiao, and L. He, Direct imaging of topological edge states at a bilayer graphene domain wall, Nat. Commun. **7**, 11760 (2016).

[40] H. Chen, P. Zhou, J. Liu, J. Qiao, B. Oezyilmaz, and J. Martin, Gate controlled valley polarizer in bilayer graphene, Nat. Commun. **11**, 1202 (2020).

[41] J. Yin, C. Tan, D. Barcons-Ruiz, I. Torre, K. Watanabe, T. Taniguchi, J. C. W. Song, J. Hone, and F. H. L. Koppens, Tunable and giant valley-selective Hall effect in gapped bilayer graphene, Science **375**, 1398 (2022).

[42] F. R. Geisenhof, F. Winterer, A. M. Seiler, J. Lenz, I. Martin, and R. T. Weitz, Interplay between topological valley and quantum Hall edge transport, Nat. Commun. **13**, 4187 (2022).

[43] J. S. Alden, A. W. Tsen, P. Y. Huang, R. Hovden, L. Brown, J. Park, D. A. Muller, and P. L. McEuen, Strain solitons and topological defects in bilayer graphene, Proc. Natl. Acad. Sci. USA **110**, 11256 (2013).

[44] See Supplemental Material at http://link.aps.org/supplemental/10.1103/PhysRevB.108.L121405 for details of the tight-binding lattice model, DFT calculations, band structures of additional materials, etc., which include Refs. [45–53].

[45] P. E. Blöchl, Projector augmented-wave method, Phys. Rev. B **50**, 17953 (1994).

[46] G. Kresse and J. Hafner, *Ab initio* molecular dynamics for liquid metals, Phys. Rev. B **47**, 558(R) (1993).

[47] G. Kresse and D. Joubert, From ultrasoft pseudopotentials to the projector augmented-wave method, Phys. Rev. B **59**, 1758 (1999).

[48] N. Marzari and D. Vanderbilt, Maximally localized generalized Wannier functions for composite energy bands, Phys. Rev. B **56**, 12847 (1997).

[49] I. Souza, N. Marzari, and D. Vanderbilt, Maximally localized Wannier functions for entangled energy bands, Phys. Rev. B **65**, 035109 (2001).

[50] N. Marzari, A. A. Mostofi, J. R. Yates, Ivo Souza, and D. Vanderbilt, Maximally localized Wannier functions: Theory and applications, Rev. Mod. Phys. **84**, 1419 (2012).

[51] A. A. Mostofi, J. R. Yates, G. Pizzi, Y. S. Lee, I. Souza, D. Vanderbilt, and N. Marzari, An updated version of wannier90: A tool for obtaining maximally-localized Wannier functions, Comput. Phys. Commun. **185**, 2309 (2014).

[52] G. Trambly De Laissardiere, D. Mayou, and L. Magaud, Localization of Dirac electrons in rotated graphene bilayers, Nano Lett. **10**, 804 (2010).

[53] P. Moon and M. Koshino, Optical absorption in twisted bilayer graphene, Phys. Rev. B **87**, 205404 (2013).

[54] J. Ahn and B.-J. Yang, Unconventional Topological Phase Transition in Two-Dimensional Systems with Space-Time Inversion Symmetry, Phys. Rev. Lett. **118**, 156401 (2017).

[55] J. Ahn, D. Kim, Y. Kim, and B.-J. Yang, Band Topology and Linking Structure of Nodal Line Semimetals with Z_2 Monopole Charges, Phys. Rev. Lett. **121**, 106403 (2018).

[56] J. Ahn, S. Park, and B.-J. Yang, Failure of Nielsen-Ninomiya Theorem and Fragile Topology in Two-Dimensional Systems with Space-Time Inversion Symmetry: Application to Twisted Bilayer Graphene at Magic Angle, Phys. Rev. X **9**, 021013 (2019).

[57] G. W. Semenoff, Condensed-Matter Simulation of a Three-Dimensional Anomaly, Phys. Rev. Lett. **53**, 2449 (1984).

[58] F. D. M. Haldane, Model for a Quantum Hall Effect without Landau Levels: Condensed-Matter Realization of the Parity Anomaly, Phys. Rev. Lett. **61**, 2015 (1988).

[59] J. M. Lee, M. Oshikawa, and G. Y. Cho, Non-Fermi Liquids in Conducting Two-Dimensional Networks, Phys. Rev. Lett. **126**, 186601 (2021).

[60] B.-B. Liu, X.-T. Zeng, C. Chen, Z. Chen, and X.-L. Sheng, Second-order and real Chern topological insulator in twisted bilayer α-graphyne, Phys. Rev. B **106**, 035153 (2022).

[61] F. Crasto de Lima, R. H. Miwa, and E. Suárez Morell, Double flat bands in kagome twisted bilayers, Phys. Rev. B **100**, 155421 (2019).